ADVANCED FUNCTIONAL MATERIALS
www.afm-journal.de

Nanoarchitecture Multi-Structural Cathode Materials for High Capacity Lithium Batteries

Dapeng Wang, Ilias Belharouak, Guangwen Zhou, and Khalil Amine*

Lithium-rich composite cathodes have been extensively investigated for lithium-ion batteries. Nanoarchitecture hydroxide precursor for these cathodes with two levels of particle agglomeration (1–2 μm and 10 μm) is produced using a co-precipitation method. Transmission electron microscopy and X-ray diffraction confirm that the precursor is a composite comprising transition metal hydroxides and Mn_3O_4. Cathode materials synthesized based on the precursor are "layered ($R\bar{3}m$)-layered ($C2/m$)-spinel ($Fd\bar{3}m$)" composite phase. The electrochemical performance of lithium cells utilizing this material as the cathode is determined to be excellent. Both the layered-layered-spinel composite structure and the nanoarchitecture morphology contribute to the electrochemical performance advantage of this material over other cathode materials.

1. Introduction

Key to the development of low-cost and high-energy/power electrochemical couples for lithium batteries is the cathode. Lithium-rich composite cathode materials have been extensively investigated since their first reports by Lu and Thackeray.[1–8] Nowadays, there is a consensus among researchers that these materials are composites comprising two layered components with an overall composition of $xLi_2MnO_3(1–x)LiMO_2$ (M is a transition metal).[9,10] Nuclear magnetic resonance[11,12] and transmission electron microscopy[13,14] studies have corroborated the existence of Li_2MnO_3-like domains (space group $C2/m$) within a predominant $LiMO_2$ layered phase (space group, $R\bar{3}m$). The major benefit of the composite structure is that upon charge to a high potential (>4.3 V), where conventional cathodes are unstable, the material remains intact through the activation of Li_2MnO_3; hence, capacities in the range of 250 mAh·g^{-1} have been achieved.[1–10] However, the composite delivers modest capacity when it is charged at high rates.[15,16] Reducing the particle size to nanoscale levels has been suggested as a means to improve the rate performance by shortening the lithium diffusion pathways.[17–20] However, nanoparticles have low packing densities and high surface area and, thus, promote side reactions.[21] Also, they are not economical because of the added synthesis cost.[17] Nanoarchitecture materials have the potential to overcome these problems without jeopardizing the advantages conferred by the nanotechnology.

In this study, we synthesized a nanoarchitecture $Ni_{0.25}Mn_{0.75}(OH)_2$ precursor by tailoring experimental conditions during a co-precipitation reaction. During the synthesis, hexagonal shaped nanoplates ("primary particles") were assembled into secondary particles ("first agglomeration") with average size of 1–2 μm, which then combined with other agglomerates ("second agglomeration") into a structure with an average size around 10 μm. The cathode material $Li_{1.5}Ni_{0.25}Mn_{0.75}O_{2+d}$ (d is the value to reflect the composite character of the material, d is 0.5 if all manganese is Mn^{4+}) was formed after lithiation.[6] This material combined the excellent rate performance endowed by the thin nanoplates and a reasonable packing density due to the macroporous structure.

2. Results and Discussion

Figure 1 shows scanning electron microscopy (SEM) images of the precursor $Ni_{0.25}Mn_{0.75}(OH)_2$. The photographs show that the precursor particles are large agglomerates (Figure 1a) composed of several secondary particles, which are typically 1 to 2 μm in size (Figure 1b). Each secondary particle is formed by hexagonal-shaped nanoplates with a thickness of about 50 nm and lateral dimensions ranging from 200 to 500 nm (Figure 1c). The hexagonal shape of each primary particle reflects the three-fold symmetry of the crystal structure of the hydroxide precursor, in agreement with powder X-ray diffraction (XRD) results. This nanoarchitecture is expected to be preserved after lithium addition, thereby accelerating lithium ion diffusion through the primary nanoplate particles. Also, it is expected that electrolyte wettability will be more effective as a consequence of the macropores that exist between the hexagonal plates. Another important advantage is that the material loading density at the level of the cell will not be sacrificed, as it would be if these nanoplates were entirely isolated.

The crystal structure of the precursor was identified with high-resolution powder XRD, as shown in **Figure 2** (note that the 2θ peak positions were recalculated based on the Cu-Kα

Dr. D. Wang, Dr. I. Belharouak, Dr. K. Amine
Chemical Sciences and Engineering Division
Argonne National Laboratory
9700 South Cass Ave. Argonne, IL 60439, USA
E-mail: belharouak@anl.gov
Dr. D. Wang, Dr. G. Zhou
State University of New York at Binghamton
Binghamton, NY, 13902, USA

DOI: 10.1002/adfm.201200536

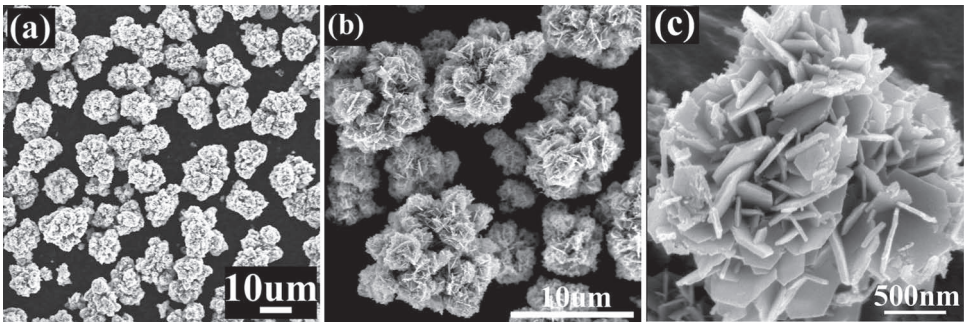

Figure 1. SEM images of hydroxide precursors: a,b) second agglomerations at different magnifications and c) first agglomeration.

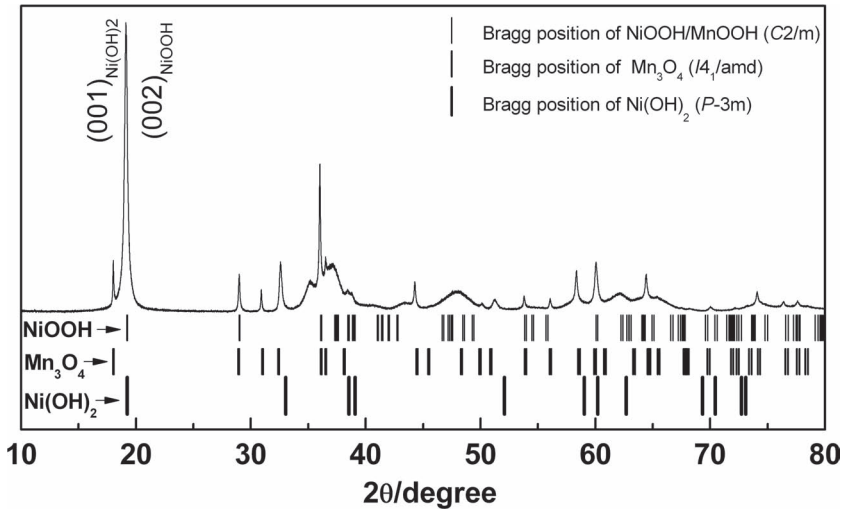

Figure 2. XRD of hydroxide precursor.

target). The main peaks of the XRD pattern were indexed based on $Ni(OH)_2$ ($P\bar{3}m$) and/or NiOOH ($C2/m$) like phases, which are the most probable structures that can form during the manganese and nickel co-precipitation. The distinction between these two possibilities led us to conduct electron diffraction on the nanoplate crystals (discussed later). The peak at 19.1° (2θ), which can be indexed to (001) for $Ni(OH)_2$-like phase or (002) for NiOOH-like phase, has the highest intensity due to the preferential crystal growth of the crystallites perpendicular to the c-axis (Figure 1c). The remaining X-ray peaks at 18°, 31°, 44.2°, and 58.3° correspond to the Bragg positions of the Mn_3O_4 tetragonal phase ($I4_1/amd$). The existence of Mn_3O_4 phase was also reported by Zhou et al. when the Mn/Ni ratio is higher than 2 for hydroxide precursors.[22] It is worth noting that our experiment yielded no layered double hydroxide (LDH), which is supported by the absence of LDH characteristic peaks at $2\theta =$ 11.5° and 22° in our precursor.[23]

Selected area electron diffraction (SAED) patterns were collected for different nanoplates (**Figure 3**). The SAED patterns in Figure 3a,b are consistent with a trigonal crystal system ($P\bar{3}m$). These patterns were collected from a crystal analyzed along the [001] zone axis (Figure 3a) and [110] zone axis (Figure

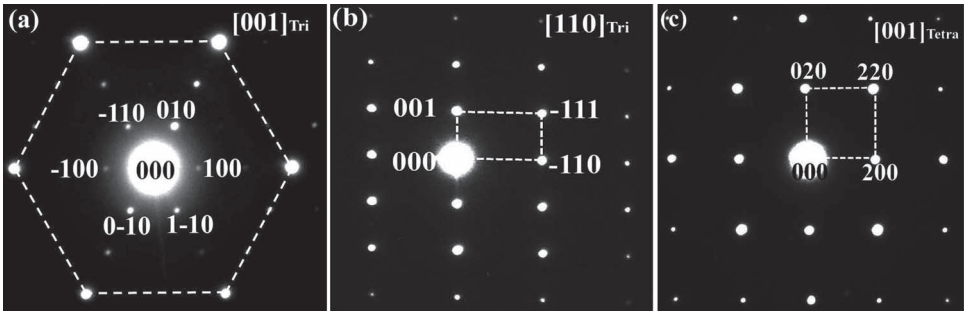

Figure 3. SAED of hydroxide precursor. Diffraction is taken from different particles and along different zone axis.

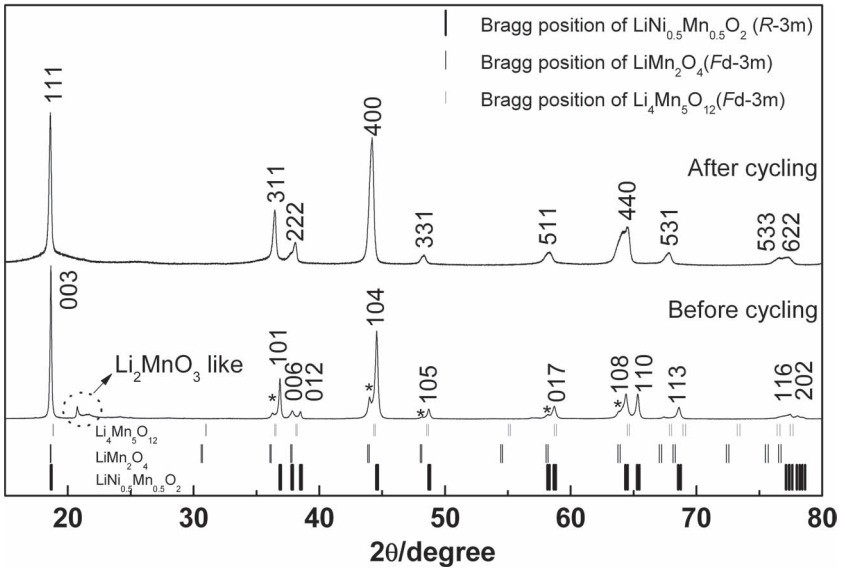

Figure 4. XRD of cathode materials before and after cycling test. Asterisks show the additional peaks corresponding to spinel structure.

3b). The SAED pattern of an adjacent particle shows a cubic motif, which could not be generated by a crystalline particle having a trigonal space group. However, the structure could also arise from a SAED pattern of a tetragonal phase ($I4_1$/amd) along the [001] zone axis. Combining the XRD and SAED findings (Figure 2,3), we can safely conclude that the precursor powder was a composite of a dominating $Ni(OH)_2$ ($P\bar{3}m$) phase and a minority Mn_3O_4 ($I4_1$/amd) phase. The existence of the Mn_3O_4 phase is due to the partial oxidation of the hydroxide precursor in air.

Next, the precursor was lithiated through a conventional solid-state reaction by its reaction with Li_2CO_3 at 900 °C, yielding a cathode material with a nominal formula of $Li_{1.5}Ni_{0.25}Mn_{0.75}O_{2+d}$. The main peaks of the material were indexed to $R\bar{3}m$ space group of $LiNi_{0.5}Mn_{0.5}O_2$ reference material[24] (**Figure 4**). The small peaks between 20° and 23° (2θ) are due to Li^+ and Mn^{2+} cation ordering in the transition metal layer, in agreement with other reports on these Mn-rich composite materials.[5,25–27] The additional peaks observed on the left side of the (101), (104), (105), (017), and (108) lines (asterisks in Figure 4) have a strong similarity with the peaks of $LiMn_2O_4$ spinel ($Fd\bar{3}m$). This observation is supported by the existence of Mn_3O_4 in the precursor, which after lithiation would have yielded $LiMn_2O_4$ spinel. Therefore, our lithiated material is a composite comprising layered-layered components plus a 4-V spinel component. We did not attribute the additional phase to $Li_4Mn_5O_{12}$ because the refined lattice parameters based on the additional peaks were $a = b = c = 8.235$ Å, which are much closer to the lattice parameters of $LiMn_2O_4$ (8.244 Å)[28] than $Li_4Mn_5O_{12}$ (8.137 Å).[29]

SEM images, transmission electron microscopy (TEM) images and the diffraction pattern of the cathode primary particles are shown in **Figure 5**. After extended calcination at 900 °C and the addition of Li^+ ions into the structure, the nanoplates developed rounded edges, shrunk in lateral dimension, and

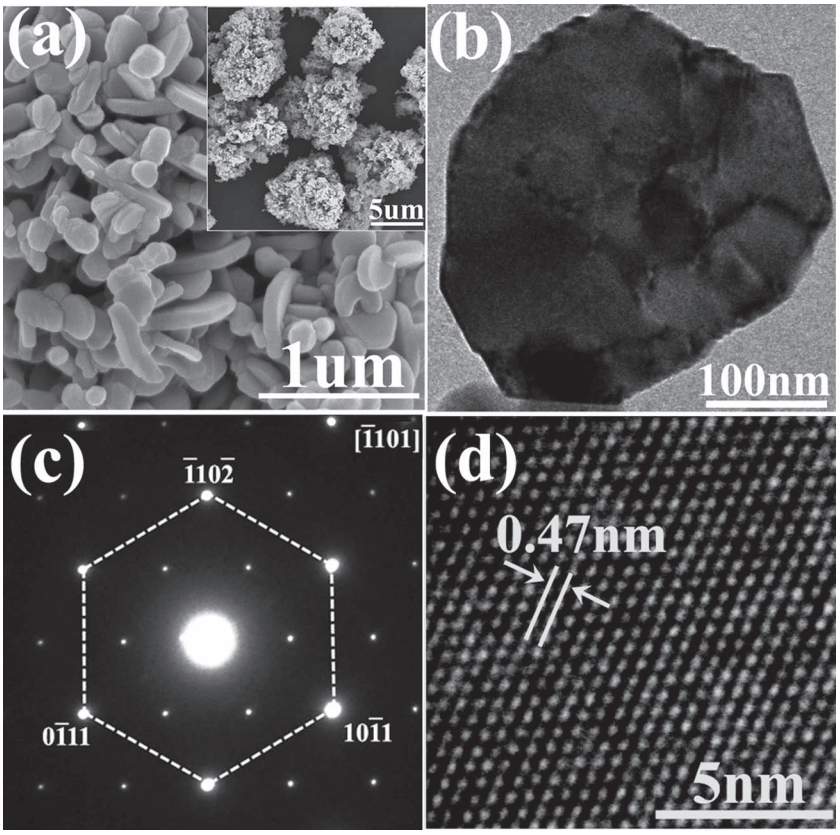

Figure 5. a) SEM images, b) TEM image, c) diffraction pattern of the cathode materials, diffraction was taken from zone axis along [$\bar{1}$101] direction, and d) high resolution TEM image.

expanded in thickness (Figure 5a). As a result, the surface area of the plate edge increased for the {110} facets, while that of the plate face decreased for the (001) facet. The increase of the edge surface area favors facile lithium diffusion through shortened plates, which is expected to enhance the rate performance of the material.[30] The inset in Figure 5a indicates that the agglomeration morphology is well kept after lithiation. Figure 5b shows a bright-field TEM image of a single nanoplate. Figure 5d exhibits a high resolution image from the selected area in Figure 5b. The lattice fringe has a distance equal to 0.47 nm, which is consistent with the expected planar distance between adjacent transition metal planes.[31] Figure 5c shows six-fold symmetry (highlighted by a dashed hexagon), which is the SAED pattern along the $[\bar{1}101]$ zone axis (indexed based on hexagonal structure) for $R\bar{3}m$ space group.

Figure S1,S2 (Supporting Information) show the particle size distribution and pore sizes of $Li_{1.5}Ni_{0.25}Mn_{0.75}O_{2+d}$, respectively. The cumulative curve and histogram curve are shown in Figure S1 (Supporting Information). The two maxima in the cumulative curve occur at 2 μm and 9 μm particle size, corresponding to the secondary particles and their agglomerates, respectively, in agreement with the SEM images. The surface area of this cathode material was 5.6 m^2/g, and the average pore size was about 25 nm (see Figure S2, Supporting Information).

The electrochemical performance of a lithium cell with $Li_{1.5}Ni_{0.25}Mn_{0.75}O_{2+d}$ electrode is shown in **Figure 6**. The rate performance of the lithium cell in the voltage window 2-4.6 V is shown in Figure 6a. The cell was initially cycled between 2 and 4.8 V for 1 cycle under a C/10 rate to activate the electrode material, and then cycled between 2 and 4.6 V at C/10, C/4, C/2, and 1C for 10 cycles per step. The initial discharge capacity at C/10 rate was slightly above 250 mAh g^{-1}, decreasing somewhat in the following 10 cycles to a discharge capacity around 225 mAh g^{-1}. The effect of current density on the specific capacity was not

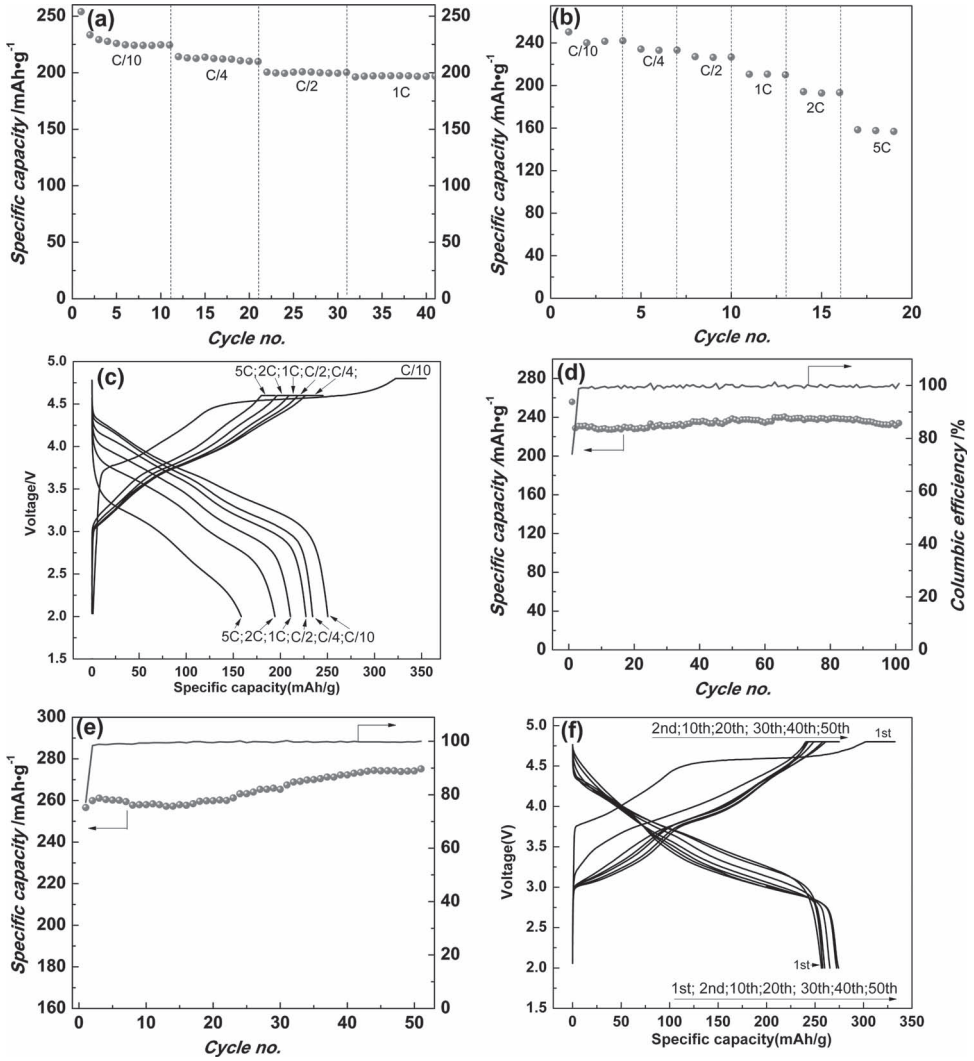

Figure 6. Rate performance of lithium cell with cathode material $Li_{1.5}Ni_{0.25}Mn_{0.75}O_{2+d}$. a) Discharge capacities under rates of C/10, C/4, C/2, and 1C in sequence for each 10 cycles. b) Discharge capacities under charge rate of C/10 and discharge rates of C/10, C/4, C/2, 1C, 2C, and 5C in sequence for each 3 cycles. c) Voltage profile for (b) under different rates. d) Cycling under charge rate of C/10 and discharge rate of 1C. e) Cycling under charge and discharge rate of C/10. f) Voltage profile for (e).

significant when the rate was raised to C/4, C/2, and 1C. The reversible capacity was 200 mAh g^{-1} at the 1 C rate.

To evaluate the cells at higher discharge rate, we eliminated the polarization in the charge process to ensure a fully charged state. Lithium cells were activated under the same condition as mentioned above; however, the C/10 rate alone was applied during the charge, while the cells were discharged at C/10, C/4, C/2, 1C, 2C, and 5C between 2 and 4.6 V with 3 cycles per step. The rate performance is shown in Figure 6b. The specific capacities at 1C, 2C, and 5C discharge rates were 211, 194, and 159 mAh g^{-1}, respectively. Obvious IR drop due to increased inner resistance of the cell is evident from the curves in the Figure 6c. These specific discharge capacities are among the highest obtained for similar materials reported in the literature.[1–7]

Because of the likelihood of electrolyte instability at high voltage and possible side reactions, we checked the cycling performance of lithium cells under the following conditions: after activation, the cell was cycled in the voltage window 2–4.8 V with a C/10 charge rate (to eliminate polarization) and a 1C discharge rate. In this case (Figure 6d), the lithium cell attained a reversible capacity of 230–240 mAh g^{-1} and maintained almost 100% capacity retention and coulombic efficiency at the completion of 100 cycles. When the lithium cell was charged and discharged at the C/10 rate between 2 V and 4.8 V, the initial discharge capacity was 255 mAh g^{-1} (Figure 6e). Surprisingly, the capacity increased for the subsequent cycles, reaching 275 mAh g^{-1} after 50 cycles; this increase is likely due to further activation of the cathode material. Note that this capacity increase was accompanied by a slight voltage drop during the discharge (Figure 6f). The columbic efficiency was almost 100%, which indicates reversible electrochemical processes rather than side reactions between electrode and electrolyte. The improved electrochemical performance in terms of capacity, rate, and cycling is linked to the macrostructure of the cathode material, which facilitated electrolyte penetration through the voids between the thin nanoplates so that lithium diffusion was favored along their lateral directions. The excellent rate performance could be due to the existence of the 4-V spinel phase initially within the composite material. On cycling, the layered cathode transformed to a spinel-like structure (Figure 4) because of the clear merger between the coupled peaks (006)/(012) and (108)/(110), which are usually used to distinguish between layered and spinel structures.[32] The spinel-like phase could have significantly improved the overall electrochemical performance of the cathode material. The observed high capacity, however, does not justify a complete transformation to a spinel phase. Therefore, we concluded this cathode is likely a composite of a layered phase that provides the high capacity and a spinel-like phase that ensures the high rate capability. These complex structural transformations are being investigated further as they could be the potential reason behind the substantial voltage profile changes during the discharge of the material under different rate and/or cycling conditions.

3. Conclusions

A nanoplate architecture precursor with multiple phases was produced by a hydroxide co-precipitation method using a continuously stirred tank reactor. After reaction with lithium carbonate at high temperature, a Li- and Mn-rich composite was synthesized with a similar morphology. Results from TEM and XRD confirmed that the precursor was a transition metal hydroxide and Mn_3O_4 composite. The hexagonal nanoplate and the layered-layered-spinel composite structure played a major role in improving the overall electrochemical performance, especially the lithium kinetics, in this cathode.

4. Experimental Section

Material Synthesis: Nickel sulfate hexahydrate ($NiSO_4 \cdot 6H_2O$), manganese sulfate monohydrate ($MnSO_4 \cdot H_2O$), sodium hydroxide (NaOH), and ammonium hydroxide ($NH_3 \cdot H_2O$) were used as the starting materials to prepare $Ni_{0.25}Mn_{0.75}(OH)_2$ precursor. These materials were mixed in the water-jacketed continuously stirred tank reactor (CSTR) system described in an earlier report.[33,34] The reaction was conducted under an inert atmosphere by bubbling N_2 into the CSTR to mitigate the oxidation of Mn^{2+} and Ni^{2+}. The precursor material was collected from hour 7 to hour 9 of the process. Collected samples were washed with hot water several times to remove residual sodium and sulfuric species, then filtered and dried inside a vacuum oven set at 80 °C over 24 h. Finally, about 600 g precursor with dark brown color was harvested.

Subsequently, $Li_{1.5}Ni_{0.25}Mn_{0.75}O_{2+d}$ cathode materials were prepared by calcining appropriate amounts of the precursor $Ni_{0.25}Mn_{0.75}(OH)_2$ and Li_2CO_3 at 900 °C for 15 h. The synthesized cathode materials were mixed with acetylene black and polyvinylidene difluoride binder with the weight ratio of 80:10:10 and coated onto an aluminum foil. Lithium cells were assembled inside a helium-filled glove box with $Li_{1.5}Ni_{0.25}Mn_{0.75}O_{2+d}$ cathode and lithium metal as the counter electrode. Celgard 2325 membrane was used as the separator. The electrolyte was $LiPF_6$ (1.2 M) dissolved in ethylene carbonate (EC) and ethyl methyl carbonate (EMC) (3:7 vol%). The cells were tested in the voltage range of 2.0–4.6 V or 2–4.8 V and different rates as discussed in Section 2. A 1C rate is equivalent to 200 mAh g^{-1} in our definition.

Characterizations: The morphologies of both of the precursor and cathode materials were characterized with cold field emission scanning electron microscopy (SEM, Hitachi S-4700-II) and transmission electron microscopy (TEM, Philips CM30T, JEOL2100). To prepare the TEM specimen, the precursor was first gently crushed with a pestle and then uniformly suspended in ethanol with the help of ultrasonic dispersion. The suspension was dropped onto a carbon-coated copper grid for TEM characterization. Particle size distributions were measured with a particle size analyzer (Cilas1090).

Powder XRD studies were performed at Argonne's Advanced Photon Source (APS), station 12-BM. A small amount of the sample was placed in a 0.33 mm Kapton capillary (0.01-mm wall thickness), filling approximately 3–5 mm of the capillary. After the capillary was sealed, experimental data were collected by a 2D image plate detector. The wavelength (λ = 0.10798 Å) and sample-to-detector distance (d = 180 mm, giving a usable range of d-spacing of 1.34–40 Å) were calibrated with CeO_2 as a reference material.

For post-cycling characterization, the above cells were disassembled in a helium-filled glove box. Then, dry powder was scratched from the cathode after washing with dimethyl carbonate and sealed in a Kapton tube for high resolution XRD characterization.

Supporting Information

Supporting Information is available from the Wiley Online Library or from the author.

Acknowledgements

This research was funded by the U.S. Department of Energy, Freedom CAR, and Vehicle Technologies Office. The electron microscopy was accomplished at the Electron Microscopy Center for Materials Research at Argonne National Laboratory. Use of the Advanced Photon Source was supported by the U.S. Department of Energy Office of Science Laboratory operated under Contract No. DE-AC02-06CH11357 by UChicago Argonne, LLC.

Received: February 23, 2012
Published online: June 14, 2012

[1] Z. Lu, D. D. MacNeil, J. R. Dahn, *Electrochem. Solid State Lett.* **2001**, *4*, A191.
[2] M. H. Rossouw, M. M. Thackeray, *Mater. Res. Bull.* **1991**, *26*, 463.
[3] S. H. Kang, Y. K. Sun, K. Amine, *Electrochem. Solid State Lett.* **2003**, *6*, A183.
[4] C. S. Johnson, J.-S. Kim, A. J. Kropf, A. J. Kahaian, J. T. Vaughey, L. M. L. Fransson, K. Edström, M. M. Thackeray, *Chem. Mater.* **2003**, *15*, 2313.
[5] M. M. Thackeray, S.-H. Kang, C. S. Johnson, J. T. Vaughey, S. A. Hackney, *Electrochem. Commun.* **2006**, *8*, 1531.
[6] H. X. Deng, I. Belharouak, R. E. Cook, H. M. Wu, Y. K. Sun, K. Amine, *J. Electrochem. Soc.* **2010**, *157*, A447.
[7] I. Belharouak, G. M. Koenig Jr., J. Ma, D. P. Wang, K. Amine, *Electrochem. Commun.* **2011**, *13*, 232.
[8] G. M. Koenig, I. Belharouak, H. X. Deng, Y. K. Sun, K. Amine, *Chem. Mater.* **2011**, *23*, 1954.
[9] C. S. Johnson, J.-S. Kim, C. Lefief, N. Li, J. T. Vaughey, M. M. Thackeray, *Electrochem. Commun.* **2004**, *6*, 1085.
[10] S.-H. Park, S.-H. Kang, C. S. Johnson, K. Amine, M. M. Thackeray, *Electrochem. Commun.* **2007**, *9*, 262.
[11] W.-S. Yoon, S. Iannopollo, C. P. Grey, D. Carlier, J. Gorman, J. Reed, G. Ceder, *Electrochem. Solid State Lett.* **2004**, *7*, A167.
[12] C. P. Grey, W.-S. Yoon, J. Reed, G. Ceder, *Electrochem. Solid State Lett.* **2004**, *9*, A290.
[13] J. Bareno, C. H. Lei, J. G. Wen, S.-H. Kang, I. Petrov, D. P. Abraham, *Adv. Mater.* **2010**, *22*, 1122.
[14] J. G. Wen, J. Bareño, C. H. Lei, S. H. Kang, M. Balasubramanian, I. Petrov, D. P. Abraham, *Solid State Ionics* **2011**, *182*, 98.
[15] S.-H. Kang, M. M. Thackeray, *Electrochem. Commun.* **2009**, *11*, 748.
[16] J. R. Croy, S.-H. Kang, M. Balasubramanian, M. M. Thackeray, *Electrochem. Commun.* **2011**, *13*, 1063.
[17] P. G. Bruce, B. Scrosati, J. M. Tarascon, *Angew. Chem. Int. Ed.* **2008**, *47*, 2930.
[18] G. Centi, S. Perathoner, *Eur. J. Inorg. Chem.* **2009**, 3851.
[19] J. Chen, F. Y. Cheng, *Acc. Chem. Res.* **2009**, *6*, 713.
[20] Y. Wang, G. Z. Cao, *Adv. Mater.* **2008**, *20*, 2251.
[21] Y.-G. Guo, J. S. Hu, L.-J. Wan, *Adv. Mater.* **2008**, *20*, 2878.
[22] F. Zhou, X. M. Zhao, A. V. Bommel, A. W. Rowe, J. R. Dahn, *Chem. Mater.* **2010**, *22*, 1015.
[23] W. B. Luo, J. R. Dahn, *Chem. Mater.* **2009**, *21*, 56.
[24] J. Breger, N. Dupre, P. J. Chupas, P. L. Lee, T. Proffen, J. B. Parise, C. P. Grey, *J. Am. Chem. Soc.* **2005**, *127*, 7529.
[25] A. D. Robertson, P. G. Bruce, *Chem. Mater.* **2003**, *15*, 1984.
[26] M. M. Thackeray, C. S. Johnson, J. T. Vaughey, N. Li, S. A. Hackney, *J. Mater. Chem.* **2005**, *15*, 2257.
[27] S.-H. Kang, S.-H. Park, C. S. Johnson, K. Amine, *J. Electrochem. Soc.* **2007**, *154*, A268.
[28] P. Strobel, F. le Cras, L. Seguin, M. Anne, J. M. Tarascon, *J. Solid State Chem.* **1998**, *135*, 132.
[29] W. Branford, M. A. Green, D. A. Neumann, *Chem. Mater.* **2002**, *4*, 1649.
[30] G.-Z. Wei, X. Lu, F.-S. Ke, L. Huang, J.-T. Li, Z.-X. Wang, Z. Y. Zhou, S.-G. Sun, *Adv. Mater.* **2010**, *22*, 4364.
[31] C. H. Lei, J. Bareno, J. G. Wen, I. Petrov, S.-H. Kang, D. P. Abraham, *J. Power Sources* **2008**, *178*, 422.
[32] S.-S. Shin, Y. K. Sun, K. Amine, *J. Power Sources* **2002**, *112*, 634.
[33] D. P. Wang, I. Belharouak, G. M. Koenig, G. W. Zhou, K. Amine, *J. Mater. Chem.* **2011**, *21*, 9290.
[34] D. P. Wang, I. Belharouak, S. Gallagher, G. W. Zhou, K. Amine, *J. Mater. Chem.* DOI: 10.1039/C2JM31285A.